



Laboratory testing and numerical simulation of properties and thermal-induced cracking of Eibenstock granite at elevated temperatures

Fei Wang¹ · Heinz Konietzky¹ · Thomas Frühwirth¹ · Yajie Dai^{2,3}

Received: 6 April 2019 / Accepted: 28 January 2020 / Published online: 11 February 2020
© The Author(s) 2021

Abstract

The knowledge about thermo-mechanical properties of granite is still limited to some extent. Individual measurements are necessary to obtain reliable properties for specific granite types. A reliable numerical model of thermal cracking behaviours of granite exposed to extreme high temperatures (e.g. 800–1000 °C) is missing. In this study, the impact of temperature up to 1000 °C on physical, mechanical, and thermal properties as well as thermo-mechanical coupled behaviour of Eibenstock granite was investigated by laboratory testing and numerical simulations. The physical properties including mineral composition, density, P-wave velocity, and open porosity are measured to be temperature dependent. Uniaxial compression and Brazilian tests were carried out to measure uniaxial compressive strength (UCS), Young's modulus, stress–strain relationship, and tensile strength of Eibenstock granite before and after thermal treatment, respectively. Thermal properties including specific heat, thermal conductivity, thermal diffusivity, and linear thermal expansion coefficient are also measured and found to be temperature dependent, especially the expansion coefficient which shows a steep increase around 573 °C as well as at 870 °C. The numerical simulation code FLAC^{3D} was used to develop a numerical scheme to simulate the thermal-induced damage of granite at high temperatures. Statistical methods combined with real mineral composition were used to characterize the heterogeneity of granite. The numerical model is featured with reliable temperature-dependent parameters obtained from laboratory tests. It can well reproduce the laboratory results in form of thermal-induced micro- and macrocracks, as well as the stress–strain behaviour and the final failure pattern of Eibenstock granite after elevated temperatures up to 1000 °C. The simulation results also reveal that the thermal-induced microcracks are randomly distributed across the whole sample. Although most thermal-induced damages are tensile failures, shear failure begins to develop quickly after 500 °C. The obvious UCS reduction in granite due to heating is mainly caused by the increase in shear failure. The simulation also shows that the dominant impact of α – β quartz transition is widening pre-existing cracks rather than the formation of new microcracks.

Keywords Granite property · Heterogeneity · Numerical simulation · Thermo-mechanical behaviour · Thermal damage

1 Introduction

Granite is often considered as potential host rock for nuclear waste disposals, tunnels, caverns, etc., and was also used as construction material for historical buildings and monuments [6, 30]. Geotechnical constructions like tunnels and historical buildings can be exposed to extreme high temperatures in case of fire accidents [31]. As a result, granites can become damaged by thermal cracking due to accumulation of internal stresses which are mainly controlled by (a) the constituents of the rocks, (b) the thermal

✉ Fei Wang
fei.wang1@student.tu-freiberg.de

¹ Geotechnical Institute, TU Bergakademie Freiberg, 09596 Freiberg, Germany

² State Key Laboratory of Refractories and Metallurgy, Wuhan University of Science and Technology, Wuhan 430081, China

³ National-Provincial Joint Engineering Research Center of High Temperature Materials and Lining Technology, Wuhan 430081, China

expansion anisotropy of individual minerals, and (c) the thermal gradients [30].

Thermal effects on physical, mechanical, and thermal properties of granite have been investigated by many scholars. However, the existing data basis is limited, because thermo-mechanical properties among different granites can show distinctly different behaviours at elevated temperatures. For example, some granites have a further jump in thermal expansion coefficient between 800 and 900 °C [8], while for some other granites the coefficient remains at a low level after 573 °C [9]. The uniaxial compressive strength (UCS) of some granites increases slightly for samples heated up to 200–400 °C and then decreases evidently at higher temperatures [3, 22]; for some other granites, the UCS shows a continuous decrease with rising temperature [9, 41]. Although Young's modulus usually decreases gradually to a much lower value after a critical temperature (about 600 °C), some granites exhibit a slight increase within a certain temperature range like 25–200 °C [5]. Therefore, individual measurements are needed to obtain reliable properties for specific granite types.

The property change is significantly influenced by micro- and macrocracks induced by thermal loading. To obtain a deeper understanding of the thermal-induced damage of granite under elevated temperatures, numerical simulation has become an important method. Previous simulations have usually applied constant properties and low or fixed temperatures [30, 35, 40]. Yang et al. [37] used a particle-based method to investigate the failure behaviour of pre-holed granite specimens after elevated temperature treatment. Although they use heterogeneous models, the mineral properties (especially the thermal expansion coefficient) are temperature independent. Yan and Zheng [36] proposed a coupled thermo-mechanical model (FDEM-TM) for simulating thermal cracking of granite, but the correctness of this model is verified only in the temperature range between 0 and 100 °C. By comparing temperature-dependent and temperature-independent rock properties applied in underground coal gasification reactor simulations, Otto and Kempka [19] found notable differences in rock failure behaviour and concluded that temperature-dependent parameters are important to obtain more reliable results. Wang and Konietzky [30] proposed a model with temperature-dependent thermo-mechanical parameters to simulate thermal cracking of granite. However, the quantitative analysis of thermal cracks is limited due to the fact that most model parameters are generalized values instead of specific laboratory-tested ones. Accurate temperature-dependent properties of granite exposed to high temperatures are necessary for building a reliable numerical model. Unfortunately, a reliable numerical model of thermal cracking of

granite exposed to temperatures up to 1000 °C is still missing so far.

To reproduce the heterogeneous nature of granite in numerical models, one method is to model spatial distribution of mineral grains based on the real mineral composition obtained from images of a real piece of rock [2, 26]. But there is an obvious drawback of such a reconstruction of three-dimensional bodies of heterogeneous materials: Only one specific configuration is duplicated. Another popular way is to use statistical methods to characterize the heterogeneity [27, 29]. However, this method lacks the factual mineral composition of the rocks, and the determination of statistical parameters relies only on the repeated back-analysis. A recently proposed methodology [32] combining Weibull functions with the real mineral composition of granite is used in this work, which overcomes the shortcomings of using existing methods for the heterogeneity characterization of rocks at the crystal-size or grain-size level.

In this study, a comprehensive investigation of physical, mechanical, and thermal properties of Eibenstock granite at temperatures up to 1000 °C was conducted in the laboratory. Numerical models considering heterogeneity and temperature-dependent properties are built to investigate the effect of high temperatures on granite. The presented approach provides a deeper understanding of the thermo-mechanical behaviour of granite after high-temperature treatment.

2 Sample preparation and test methods

The investigated granite is from the Eibenstock Massiv in Saxony, Germany. Mechanical and physical properties of granite were determined at room temperature (25 °C) before and after the heating process. Thermal properties were measured according to an elaborated heating scheme with a minimum repetition of 3 specimens for each individual treatment. Except for the test of thermal conductivity, all the other laboratory tests were conducted in the rock mechanical laboratory at TU Bergakademie Freiberg, Germany [33].

According to the ISRM recommendations, cylindrical samples (50 mm diameter and 110 mm length) were prepared for determination of UCS, Young's modulus, density, and porosity. The Brazilian discs with a nominal diameter of 50 mm and a thickness of 25 mm are used to determine the indirect tensile strength of granite which experienced different temperatures.

In addition to the specimens investigated at room temperature, cylindrical granite specimens were heated up to 400 °C, 600 °C, 800 °C, and 1000 °C with a heating rate of 5 °C/min. The specimens are kept at target temperatures

for 36 h to guarantee homogeneous temperature distribution and deformation equilibrium. Subsequently, specimens are cooled down to room temperature at a rate of 1 °C/min. The heating scheme applied for the Brazilian tests is the same as for the cylindrical specimens.

The temperature-dependent bulk density ρ is tested by measuring the volume V (i.e. diameter D and length L) and mass M of the cylindrical specimens at room temperature and after the temperature treatment. The bulk densities are calculated by using Eq. (1):

$$\rho = \frac{M}{V} = \frac{4M}{\pi D^2 L} \quad (1)$$

To investigate the evolution of the failure process induced by the heating treatments, p-wave velocity and open porosity of the fresh and thermal damaged granite samples are measured. For p-wave velocity measurement, two piezo-electric sensors are used as source and receiver, respectively. The sensors are centrally located at the top and bottom end surface of the sample. P-wave velocity is calculated by dividing distance by travel time of the primary ultrasonic impulse. The open porosity Φ_0 is determined using the procedure defined by DIN EN 1936 [4], according to the following formula:

$$\Phi_0 = (m_s - m_d)/(m_s - m_h) \times 100 \quad (2)$$

where m_s is the water-saturated mass, m_h is the mass suspended in water, and m_d is the oven-dry mass.

To determine the coefficient of linear thermal expansion, four granite samples with a diameter of 5 mm and nominal length of 20 mm were heated up to 1000 °C at 5 °C/min. The test was conducted with a dilatometer at the Institute of Ceramic, Glass and Construction Materials at TU Bergakademie Freiberg. The thermal diffusivity, thermal conductivity, and specific heat capacity were measured using a NETZSCH Laser Flash Apparatus LFA 457 at Wuhan University of Science and Technology, China. The nominal specimen dimension of the three discs is 12.5 mm in diameter and 2.5 mm in thickness. Thermal diffusivity and specific heat were determined by the laser flash device. The thermal conductivity is calculated by the following equation:

$$\lambda(T) = \kappa(T) \cdot C_p(T) \cdot \rho(T) \quad (3)$$

where λ is the thermal conductivity [W/(m K)], κ is the thermal diffusivity (mm²/s), C_p is the specific heat [J/(g K)], ρ is the bulk density (g/cm³).

Uniaxial tests were performed at room temperature after heat treatment. The specimens were uniaxially compressed with a rate of 0.1 mm/min. The Brazilian discs were compressed with 0.05 mm/min to obtain the tensile strength of the granite specimen experienced elevated temperatures according to following equation:

$$\sigma_t = \frac{2P_{\max}}{\pi DB} \quad (4)$$

where P_{\max} is the maximum load, D is the diameter of the disc, and B is the thickness of the disc.

3 Laboratory test results

3.1 Physical properties

3.1.1 Mineral composition

Figure 1 shows the mineral composition of Eibenstock granite. The grains have irregular shapes like fan-shaped, strip-shaped, xenomorphic, etc. The grain size also varies significantly. Orthoclase accounts for a large share of mineral composition with a proportion of 40%. The minerals usually have a grain size between 1 mm and 4 mm, though some grains show the maximum and minimum size of 7 mm and 0.04 mm, respectively. It was found that different grain sizes results in different stress concentrations within the rock, which can eventually affects the strength of the rock [38]. This effect can also lead to different crack patterns when the granite is exposed to heating–cooling treatments [23]. Plagioclase accounts for 10% of minerals and usually concentrates in individual areas compared to other detectable minerals. Quartz has a mineral proportion of 44%, which is very close to the value for orthoclase. The maximum quartz grain size ranges from 1.5 to 4.8 mm. Siderophyllite grains are usually scaly and xenomorphic and account for 6% of the mineral composition. The largest mineral grains reach a diameter of 3.5 mm, whereas the smallest have a size of 0.02 mm. Besides the minerals mentioned above, accessory minerals account for less than 1%.

3.1.2 Density

Table 1 documents the dimensions and mass changes of granite after the heat treatments. Figure 2a shows the density development according to Table 1. The average density of Eibenstock granite at room temperature is 2.60 g/cm³. The density decreases slightly to 2.58 g/cm³ at 400 °C, and to 2.54 g/cm³ at 600 °C. An obvious decrease happens at 1000 °C where the density drops to 2.20 g/cm³ due to the significant increase in specimen volume (see Fig. 2b). Compared with the volume change, the mass change is very small (see Fig. 2b) and can mainly be attributed to the loss of chemically combined water.

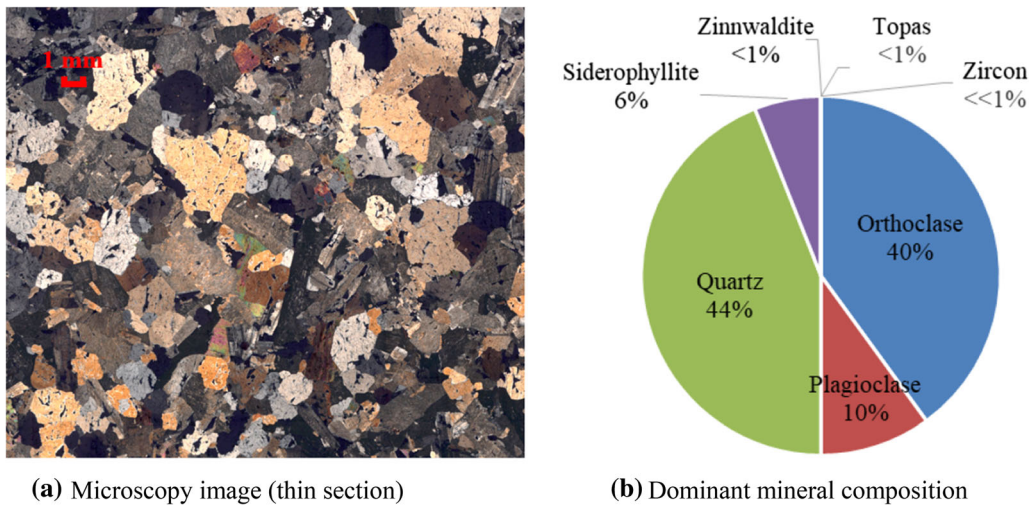


Fig. 1 Mineral composition of Eibenstock granite

Table 1 Dimensions and mass changes of granite after heat treatment

Nos.	25 °C			Target temperature		
	Diameter (mm)	Height (mm)	Mass (g)	Diameter (mm)	Height (mm)	Mass (g)
400-1	49.63	109.81	553.11	49.67	109.92	550.11
400-2	49.68	109.69	553.60	49.73	109.77	550.38
400-3	49.67	109.46	552.60	49.71	109.54	549.59
600-1	49.67	109.04	550.78	49.95	109.69	545.98
600-2	49.68	108.75	549.35	49.95	109.39	544.57
600-3	49.69	109.67	553.73	49.96	110.37	548.77
1000-1	49.65	109.62	552.26	52.38	115.53	546.77
1000-2	49.69	109.94	555.32	52.20	115.91	545.66
1000-3	49.65	109.84	552.72	52.21	115.64	545.65

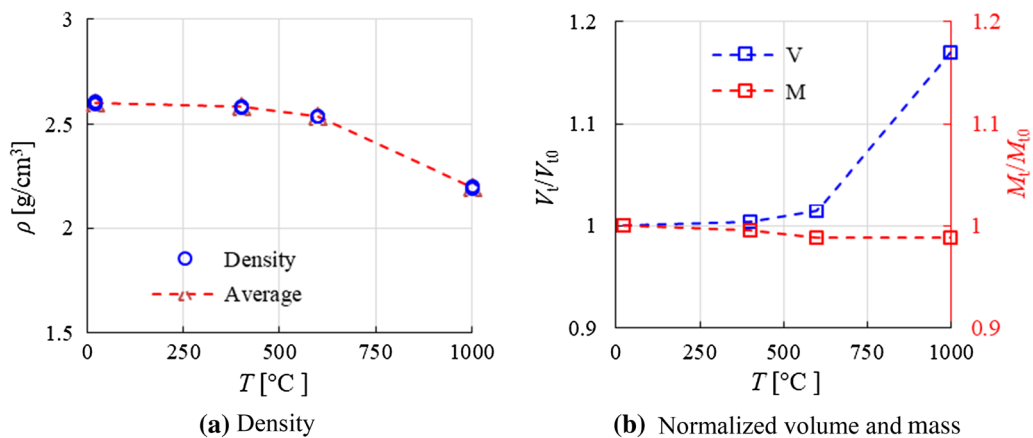


Fig. 2 Volume and mass variation for different temperatures. V_t and M_t are the volume and mass at target temperatures, while V_{t0} and M_{t0} correspond to room temperature

3.1.3 P-wave velocity

The evolution of p-wave velocity (V_p) for samples at different temperatures is shown in Fig. 3. It can be seen that the p-wave velocity decreases with temperature rising, especially at 600 °C where the velocity shows the most significant reduction. From room temperature to 400 °C, the velocity reduces from 4263 to 2914 m/s; then it drops to 1355 m/s at 600 °C and continuously decreases to only 526 m/s at 1000 °C. The open porosity is plotted in Fig. 3. Up to 600 °C, the open porosity shows an opposite trend with P-wave velocity. However, the porosity increasing step is most significant in the temperature range of 600–1000 °C, while the P-wave velocity reduction is not so pronounced in this temperature range (see Fig. 3). The P-wave velocity is affected by the total material damage, while the open porosity can only reflect the network of connected cracks. Therefore, we can deduce that while below 600 °C primarily new, but isolated cracks are developed, these cracks are connecting at temperatures above 600 °C and generation of newly developed cracks is decelerating.

3.2 Mechanical properties

3.2.1 UCS and peak axial strain

The uniaxial compression test results are plotted in Fig. 4a and documented in Table 2. Average peak stress σ_c and corresponding strain ε_c as function of temperature are shown in Fig. 4b. UCS experiences a slight increase at 400 °C. This hardening behaviour is caused by several phenomena: compaction and crack closure induced by thermal expansion of the mineral grains; evaporation of the pore water in the rock microstructure or reduction in pre-existing cracks due to partial melting and re-crystallization of minerals [31]. Afterwards, the value decreases gradually

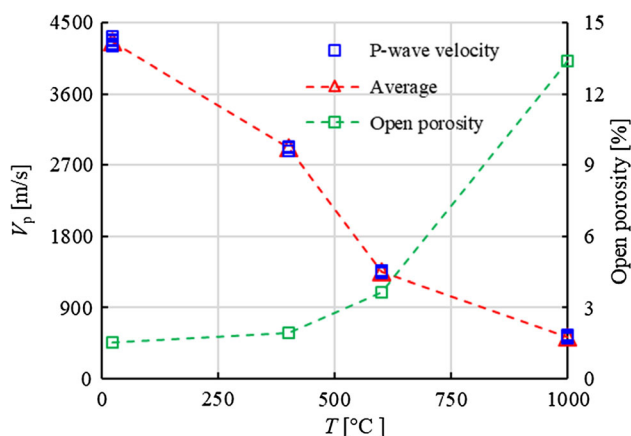


Fig. 3 Temperature-dependent P-wave velocity

up to 1000 °C due to continuously developed cracks induced by higher temperatures. Slightly different from the UCS, the peak axial strain shows a continuous increase. The stress–strain curves show gradual nonlinear behaviour from 400 to 1000 °C before reaching peak stress. The samples at 800 °C and 1000 °C display obviously ductile behaviour, which is characterized by gradual loss of strength with ongoing deformation in post-peak-phase (strain softening). The loss of brittleness and increasing ductile behaviour are associated with the increase in cracks density in the specimen [30].

3.2.2 Elastic modulus

The stiffness of the granite can be represented by the threshold Young's modulus E_c , which is defined by $E_c = \sigma_c / \varepsilon_c$ (see Table 2). The often used tangent Young's modulus E_t , which is measured at a stress level equal to 50% of UCS [12], is also calculated. Figure 5 shows E_c and E_t of granite after heat treatments. Although the general trend of both, E_c and E_t is decreasing with increasing temperature, there are differences in magnitude. E_t increases slightly at 400 °C before it decreases to a much lower level at 1000 °C, while E_c shows a continuous decrease. The maximum difference between E_c and E_t reaches 10 GPa at 400 °C.

The tangent modulus is calculated from the linear part (elastic stage) of the stress–strain curve, which is suitable to evaluate the stiffness of granite before heating. (The linear part is dominant before yielding.) However, the strong nonlinearity of the stress–strain curve at higher temperatures (see Fig. 4a) makes the determination of a Young's modulus as an elastic constant questionable [30]. The threshold modulus obtained from dividing peak axial stress by peak axial strain considers the deformation of the sample during the whole compressive loading process. Due to the larger proportion of the nonlinear part and its smaller stress/strain ratio, the threshold modulus is normally smaller than the tangent modulus [31]. The tangent Young's modulus at high temperatures might cause problems in engineering practice, since it can overestimate the stiffness of the material at higher temperatures; the threshold modulus, which can better quantify the stiffness of granite at high temperatures during the whole process until final failure, seems to be more practical [31].

3.2.3 Tensile strength

The indirect tensile strength of Eibenstock granite at room temperature is 7.8 MPa (see Fig. 6). It shows a decrease at elevated temperatures, reducing by nearly 25% at 400 °C compared with samples not heated. Due to the α – β quartz transition, the variation of tensile strength with increasing

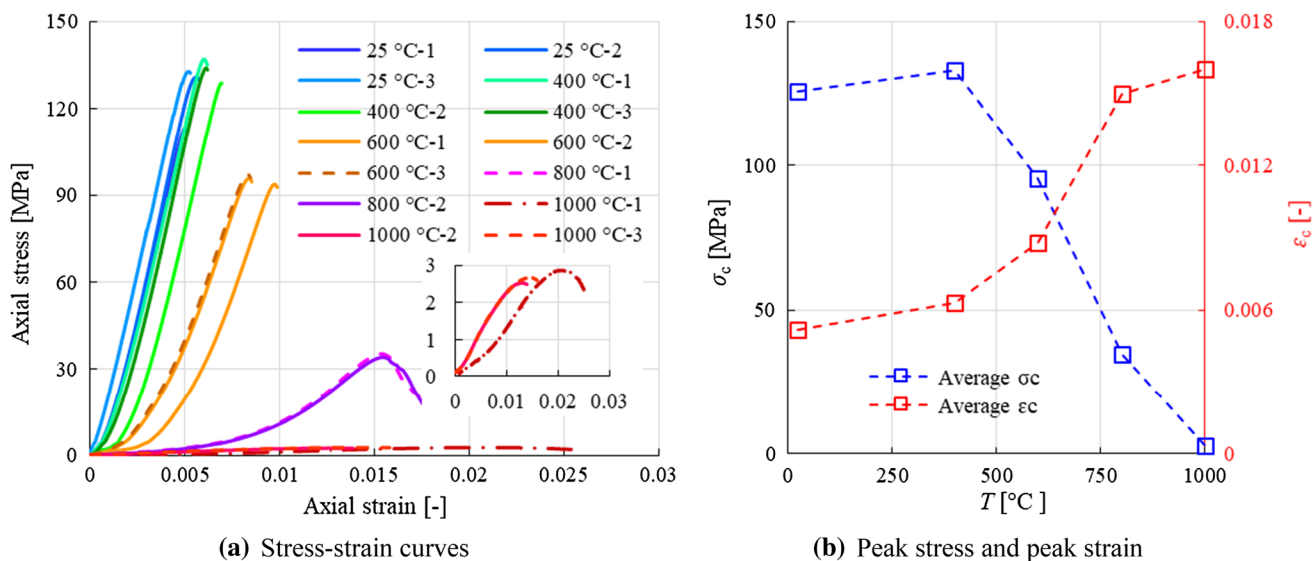


Fig. 4 Uniaxial compression test results of granite after heat treatment

Table 2 Uniaxial compression test results of granite at different temperatures

T (°C)	σ_c (MPa)	Average σ_c (MPa)	ϵ_c (-)	Average ϵ_c (-)
25	113.37	125.66	0.0050	0.0052
	130.83		0.0056	
	132.78		0.0052	
400	137.05	133.26	0.0060	0.0063
	128.78		0.0069	
	133.96		0.0061	
600	93.69	95.47	0.0097	0.0088
	95.74		0.0084	
	96.98		0.0083	
800	35.33	34.76	0.0154	0.015
	34.20		0.0154	
1000	2.86	2.68	0.0201	0.016
	2.53		0.0125	
	2.66		0.0143	

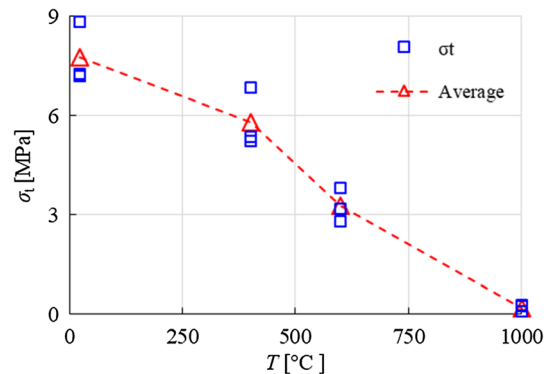


Fig. 6 Tensile strength of granite after heat treatment

temperatures is highest at about 573 °C [30]. Tensile capacity of the granite nearly vanishes after a temperature treatment of 1000 °C, because thermal-induced cracks have developed throughout the whole sample (see Fig. 15).

3.3 Thermal properties

3.3.1 Specific heat, thermal conductivity, and thermal diffusivity

Figure 7 shows specific heat (Fig. 7a), thermal conductivity (Fig. 7b), and thermal diffusivity (Fig. 7c) measured by the laser flash apparatus. The specific heat capacity shows a continuous increase with temperature from 0.706 J/(g K) at 25 °C to 0.912 J/(g K) at 600 °C. Afterwards, it decreases slightly to 0.895 J/(g K) at 800 °C. Thermal conductivity and thermal diffusivity show a similar trend and decrease monotonically with rising temperature. At room temperature, thermal conductivity of the tested granite is 3.65 W/

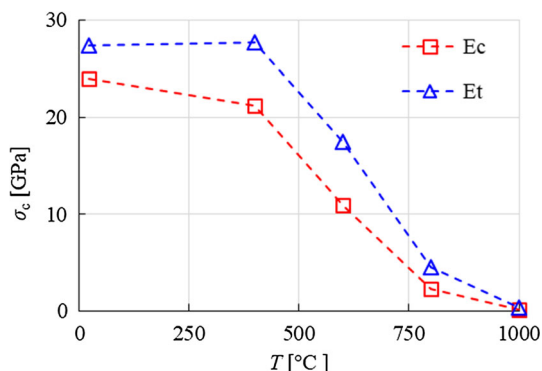


Fig. 5 Elastic modules of granite after heat treatment

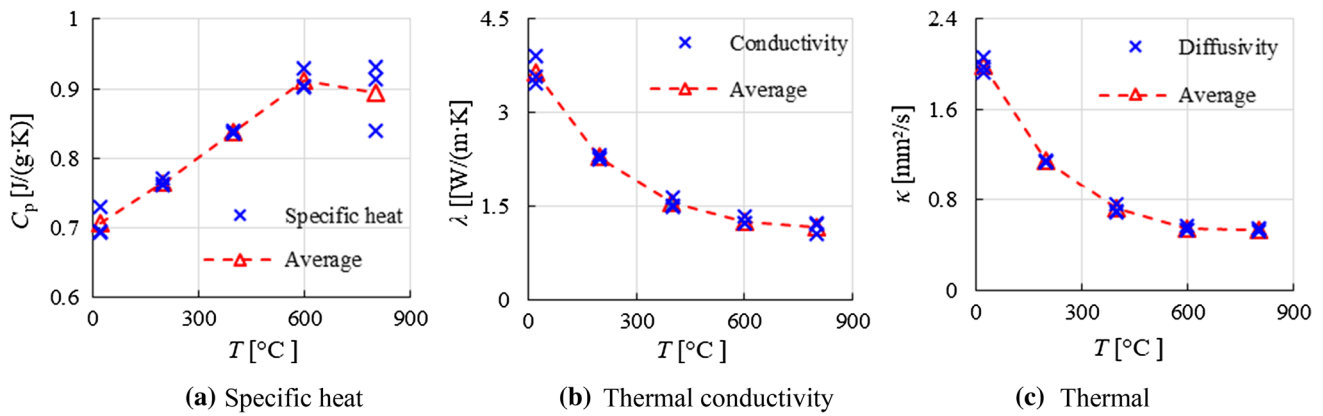


Fig. 7 Thermal properties measured by the laser flash apparatus

(m K). At higher temperatures, especially for temperatures higher than 600 °C, thermal conductivity decreases much slower and approaches a nearly constant value of approximately 1.2 W/(m K). Similar, the thermal diffusivity diminishes from 2.0 mm²/s at room temperature to some 0.5 mm²/s at 600 °C and 800 °C. The reason why thermal diffusivity and thermal conductivity approach constant values at high temperatures is been explained by Wen et al. [34]: Thermal diffusivity is connected with the number of phonons within the primitive unit cell, and an increasing temperature no longer significantly changes the number of phonons when temperature is high enough; the phonons being limited in space with a constant lattice size, and the mean free phonon path no longer decreases with increasing temperatures, which limits the thermal conductivity values of the rocks at high temperatures.

3.3.2 Linear thermal expansion coefficient

The formulas for calculating the thermal expansion coefficient can be grouped into two categories, depending on whether the expansion relates to a temperature range or a

single temperature [14]. The most general definition of average coefficient of linear thermal expansion over a temperature range is:

$$\alpha_m = \frac{(L_2 - L_1)/L_0}{T_2 - T_1} = \frac{1}{L_0} \frac{\Delta L}{\Delta T} \tag{5}$$

where L_0 is the initial length of specimen at temperature T_0 which expands to L_1 at T_1 and then to L_2 at T_2 , and ΔL is the change in length for the temperature change ΔT .

The true coefficient of linear thermal expansion is related to the derivative dL/dT at a single temperature, and it can be defined as follows [14]:

$$\alpha_T = \frac{dL/L}{dT} = \frac{1}{L} \frac{dL}{dT} \tag{6}$$

Based on the equations above, the average coefficient over a temperature range of 25 °C at target temperature (Fig. 8a) and the true coefficient at a single temperature (Fig. 8b) are plotted. The coefficient defined over a temperature range is significantly different from that defined at a single temperature. This difference will have an important implication if used in numerical models and engineering applications. Since TM-coupled calculations use

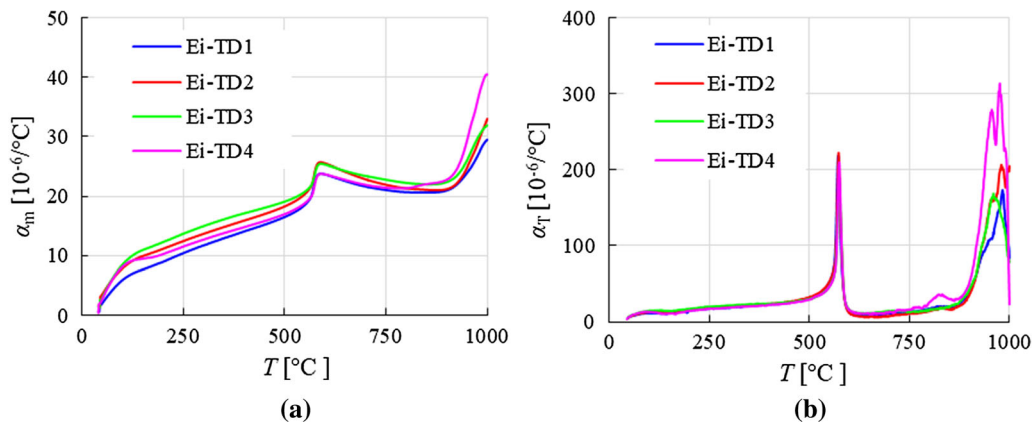


Fig. 8 Linear thermal expansion coefficient of granite after heat treatment: **a** average over 25 °C and **b** for single temperature

the parameters at a certain temperature, we only use the true coefficient in the numerical models presented in this study. It reveals that the coefficient of linear thermal expansion shows the first sharp increase around 573 °C and experiences a second increase in the range between 870 and 980 °C.

The thermal expansion coefficient increases sharply at around 573 °C due to phase transition of quartz, which will lead a large irreversible increase in volume [9, 30]. However, the knowledge about the second increase in thermal expansion between 800 and 900 °C is still limited. This behaviour could be related to the future phase transition of quartz to hexagonal tridymite at about 800 °C [8]. But the tridymite transition does only occur for quartz crystals with certain impurities, and differential thermal analysis (DTA) does not indicate such a phase change [8, 30].

4 Model set-up

4.1 Geometry and boundary conditions

A cylindrical sample (Fig. 9a) with a radius of 25 mm and a length of 110 mm is created in FLAC^{3D} [13]. The corresponding Brazilian disc with a diameter of 50 mm and a thickness of 25 mm is shown in Fig. 9b. The cylinder and disc consist of 21,600 and 16,128 elements, respectively. The length of model elements varies between 0.5 and 3.2 mm. This size is about the same as those of the

validated models for different granites developed in previous studies [30, 32]. The constitutive law used in this study is a Mohr–Coulomb model with strain softening and tension cut-off in combination with temperature-dependent adjustment of parameters [30]. The heat flux is applied to all surfaces of the samples. The cylindrical sample and Brazilian disc are fixed at the bottom in XY and XZ planes which are perpendicular to gravity directions during heating process. The heating rate is the same as during the laboratory tests (i.e. 5 °C/min). Once the target temperature is reached, the sample is continuously kept at target temperature until the temperature is uniformly distributed across the whole sample. The cooling process has an influence on the thermal cracking of granite after heat treatment [7]. However, the reduction in mechanical properties during slow heating–cooling cycles appears to be relatively small compared to continuous heating, and little structural damage occurs during the cooling phase of a thermal cycle [15, 39]. Therefore, we assume that the influence of slow cooling can be neglected. Shutting-off the thermal option is chosen to simulate the mechanical loading up to failure at room temperature [30].

During the uniaxial compression test, a low velocity (1×10^{-8} m/s) is applied at the bottom and top of the cylindrical sample (see Fig. 9a). A lower velocity (1×10^{-9} m/s) is applied at the upper and lower jaws during Brazilian tensile test (see Fig. 9b). The radius of jaws is $1.5 \times$ specimen radius, and the width of jaws is $1.1 \times$ specimen thickness [11]. The loading jaws are

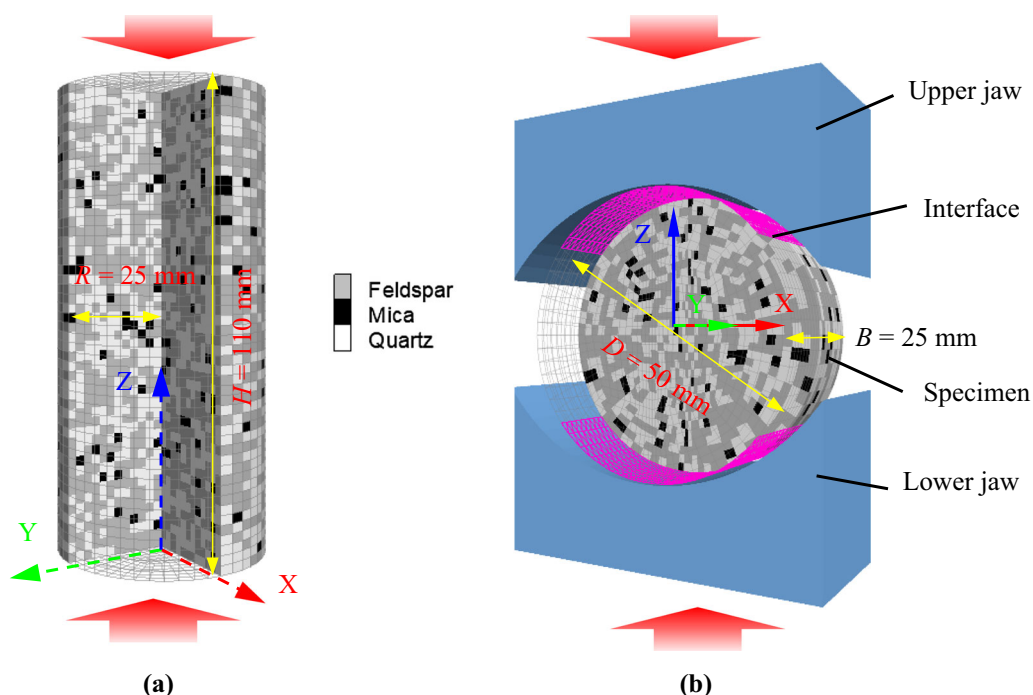


Fig. 9 Numerical model set-up

elastic with a bulk and shear modulus of 160 GPa and 80 GPa, respectively. Interfaces are also created to join the two sub-grids of the loading apparatus and the specimen to simulate an automatic contact during the loading process (see Fig. 9b). The normal stiffness (k_n) and shear stiffness (k_s) of the interfaces at room temperature are set as 1×10^{14} Pa. The model elements are divided into feldspar, quartz, and mica randomly, and the mineral proportions are 50%, 44%, and 6%, respectively.

4.2 Statistical distribution parameters for heterogeneity characterization

Weibull distribution has been considered to characterize the heterogeneity. In this study, we set the mean of Weibull random variables as 1 [17, 27], and the scale parameter x_0 and variance $\text{Var}(x)$ of Weibull distribution will become:

$$x_0 = \frac{1}{\Gamma(1 + 1/m)} \tag{7}$$

$$\text{Var}(x) = \left[\frac{1}{\Gamma(1 + 1/m)} \right]^2 \left[\Gamma\left(1 + \frac{2}{m}\right) - \Gamma^2\left(1 + \frac{1}{m}\right) \right] \tag{8}$$

where m is the shape parameter (also called homogeneity index) describing the scatter of x , Γ is the Gamma function.

The scatter characteristics of the mineral properties can be described by the variance σ_x^2 (see Table 3). The variance σ_x^2 of discrete random variable x can be calculated by:

$$\sigma_x^2 = \sum_{i=1}^n p_i (x_i - \mu_x)^2 \tag{9}$$

where p_i is the probability of discrete random variable x_i , μ_x is the mean of discrete random variables.

We set $\text{Var}(x)$ of the Weibull distribution equal to σ_x^2 of the granite minerals, and the Weibull parameters based on the mineral composition are obtained according to Eqs. (8) and (9) (see Table 3).

Table 4 Model parameters at room temperature

Parameters	P_0
Coefficient of linear thermal expansion α_{t0} (1/K)	4.94×10^{-6}
Specific heat C_{v0} (J/kgK)	706
Thermal conductivity k_0 (W/mK)	3.65
Young’s modulus E_0 (GPa)	27.38
Poisson’s ratio ν_0	0.26 [25]
Tensile strength σ_{t0} (MPa)	10.0
Cohesion c_0 (MPa)	25.5 [25]
Friction angle φ_0 (°)	53.7 [25]
Density ρ_0 (kg/m ³)	2604

This methodology overcomes the shortcomings of using existing methods for the heterogeneity characterization of rocks at the crystal-size or grain-size level. A detailed analysis and introduction of this heterogeneous method can be found in [32].

4.3 Temperature-dependent parameters

Normalized property values P_T/P_0 relate the values at certain temperature (P_T) to the value at room temperature (P_0). Based on the laboratory test results, the granite properties at room temperature and the normalized equations of temperature-dependent properties are obtained and documented in Tables 4 and 5, respectively.

The model is based on a strain-softening constitutive law, in which cohesion c and tensile strength σ_t soften after the onset of plastic yield. The softening behaviour for cohesion and tension is provided by user defined functions in the form of tables and each table contains pairs of values: one for the plastic strain, and one for the corresponding property value [13]. In this work, the table relating tension limit to plastic tensile strain is $(0, \sigma_{t0} \cdot x_i)$ ($\epsilon^{t1}, \sigma_{ti}(T)$) ($\epsilon^{t2}, 0$), while the table relating cohesion to plastic shear strain is $(0, c_0 \cdot x_i)$ ($\epsilon^{s1}, 0.5c_i(T)$) ($\epsilon^{s2},$

Table 3 Mineral properties and corresponding Weibull parameters

Mineral ^c	α_t ($10^{-6}/K$)	C_v (J/kg K)	K (W/m K)	E (GPa)	Φ (°)	C (MPa)	ν	σ_t (MPa)	P (kg/m ³)	$Pct.$ (%)
Quartz	11.5 ^a	700	7.69	81	60	50	0.16	13	265	44
Feldspar	5.0 ^b	630	2.31	52	50	40	0.19	12	2570	50
Mica	13.3 ^a	520	2.15	25	30	25	0.22	8	3120	6
$\text{Var}(x) = \sigma_x^2$	0.056	0.0054	0.329	0.072	0.020	0.024	0.010	0.0091	0.002	
M	2.7	16.8	1.8	4.2	8.3	7.7	12.1	12.7	25.8	
x_0	1.12	1.03	1.12	1.1	1.05	1.06	1.04	1.04	1.02	

^aRef. [24]

^bRef. [21, 28]

^cThe mineral properties used for calculating the Weibull parameters are from the data collection given in [32]

Table 5 Temperature-dependent property equations

Property of element <i>i</i>	Temperature-dependent equation (in normalized form)
$\rho_i(T) = \rho_0 \cdot x_i \cdot f_{\rho i/\rho_0}$	$f_{\rho i/\rho_0} = 1.00191 / (1 + e^{-6.484 + 0.00487T})$, $0^\circ\text{C} < T \leq 1000^\circ\text{C}$
$E_i(T) = E_0 \cdot x_i \cdot f_{E i/E_0}$	$f_{E i/E_0} = 1 / (1 + e^{-6.250714 + 0.010708T})$, $0^\circ\text{C} < T \leq 1000^\circ\text{C}$
$\sigma_{ti}(T) = \sigma_{t0} \cdot x_i \cdot f_{\sigma t i/\sigma_{t0}}$	$f_{\sigma t i/\sigma_{t0}} = 1 - 1.1827^{3.115} / (608.213^{3.115} + T^{3.115})$, $0^\circ\text{C} \leq T \leq 1000^\circ\text{C}$
$\nu_i(T) = \nu_0 \cdot x_i \cdot f_{\nu i/\nu_0}$ (–)	$f_{\nu i/\nu_0} = \begin{cases} -7 \times 10^{-4}T + 1.0052, & 0^\circ\text{C} \leq T \leq 600^\circ\text{C} \\ 2.240 / (1 + e^{13.11 - 0.0207T}), & 600^\circ\text{C} < T \leq 800^\circ\text{C} \end{cases}$ [32]
$c_i(T) = c_0 \cdot x_i \cdot f_{c i/c_0}$	$f_{c i/c_0} = \begin{cases} 0.003T + 0.9933, & 0^\circ\text{C} \leq T \leq 400^\circ\text{C} \\ 1 \times 10^{-6}T^2 - 0.0008T + 1.606, & 400^\circ\text{C} < T \leq 800^\circ\text{C} \\ -0.0012T + 1.22, & 800^\circ\text{C} < T \leq 1000^\circ\text{C} \end{cases}$
$\alpha_{Ti}(T) = \alpha_{T0} \cdot x_i \cdot f_{\alpha T i/\alpha_{T0}}$	$f_{\alpha T i/\alpha_{T0}} = \begin{cases} (2.5138 - 0.00039T) / (1 - 0.0025T + 1.324 \times 10^{-5}T^2), & 0^\circ\text{C} < T \leq 573^\circ\text{C} \\ 1 / (198.23327 - 0.690845T + 6.01976 \times 10^{-4}T^2), & 573^\circ\text{C} < T \leq 600^\circ\text{C} \\ 4.3797 + 2.3956 \cos(0.00905T - 2.798), & 600^\circ\text{C} < T \leq 887^\circ\text{C} \\ 22.731979 + 18.773112 \cos(0.02618T - 0.826438), & 887^\circ\text{C} < T \leq 980^\circ\text{C} \\ 991.42 - 0.97T, & 980^\circ\text{C} < T \leq 1000^\circ\text{C} \end{cases}$
$C_{vi}(T) = C_{v0} \cdot x_i \cdot f_{C v i/C_{v0}}$	$f_{C v i/C_{v0}} = \begin{cases} 0.0005T + 0.9856, & 0^\circ\text{C} \leq T \leq 600^\circ\text{C} \\ 1.27, & 600^\circ\text{C} < T \leq 1000^\circ\text{C} \end{cases}$
$\lambda_i(T) = \lambda_0 \cdot x_i \cdot f_{\lambda i/\lambda_0}$	$f_{\lambda i/\lambda_0} = 0.174 + 0.897 \times 0.9963^T + 0.00013T$, $0^\circ\text{C} \leq T \leq 1000^\circ\text{C}$

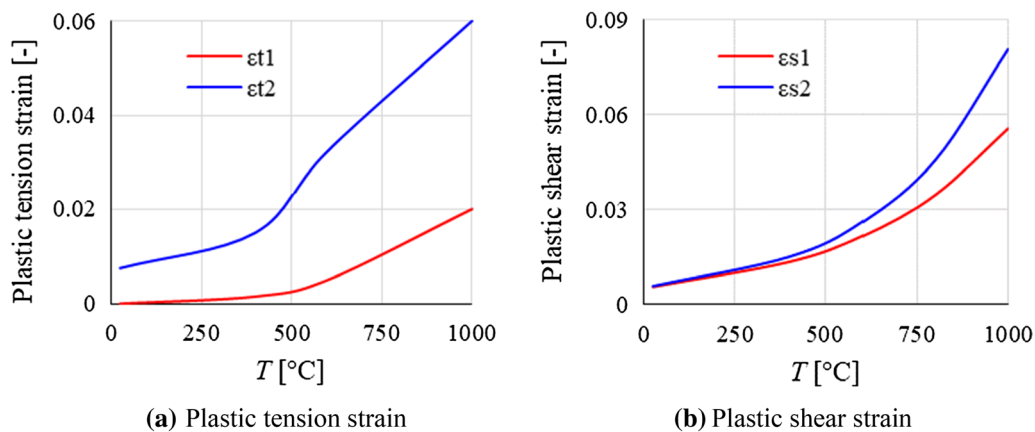


Fig. 10 Temperature-dependent parameters for softening tables

$0.2c_i(T)$). Plastic shear strain (ϵ^s) and tensile strain (ϵ^t) of each element are defined as shown in Fig. 10.

Based on Tables 3, 4, 5, and Fig. 10, the properties of granite samples are assigned to corresponding mineral grains. Fig. 11 illustrates the distribution of tensile strength and linear thermal expansion coefficient of different mineral grains at room temperature. Since the dominant variation of thermal expansion coefficient of granite is caused by the α - β quartz transition, which will lead to significant volumetric expansion [18, 20], the expansion coefficient of quartz grains follows the temperature dependence given in Table 5. Considering that the proportion of mica is very small (only 6%) and that the thermal expansion coefficients of some micas can become extraordinary high around 600 °C [10], the thermal expansion coefficient of mica also follows the equation given in Table 5 for simplicity. The

thermal expansion variation of feldspars is relatively small and experiences an increase by a factor of 1.7 in the temperature range from 298 K to 900 K [18, 28]. This trend is implemented in the numerical model as temperature-dependent expansion coefficient for feldspar.

4.4 Simulation results

4.4.1 Thermal-induced cracks

Before mechanical loading, no obvious cracks caused by thermal stresses only are observed directly in the temperature range between 25 and 800 °C. However, the samples experienced 1000 °C heat treatment show obvious macro-cracks which can be observed by the naked eye (see Fig. 12a, c). Although these cracks appear isolated, they

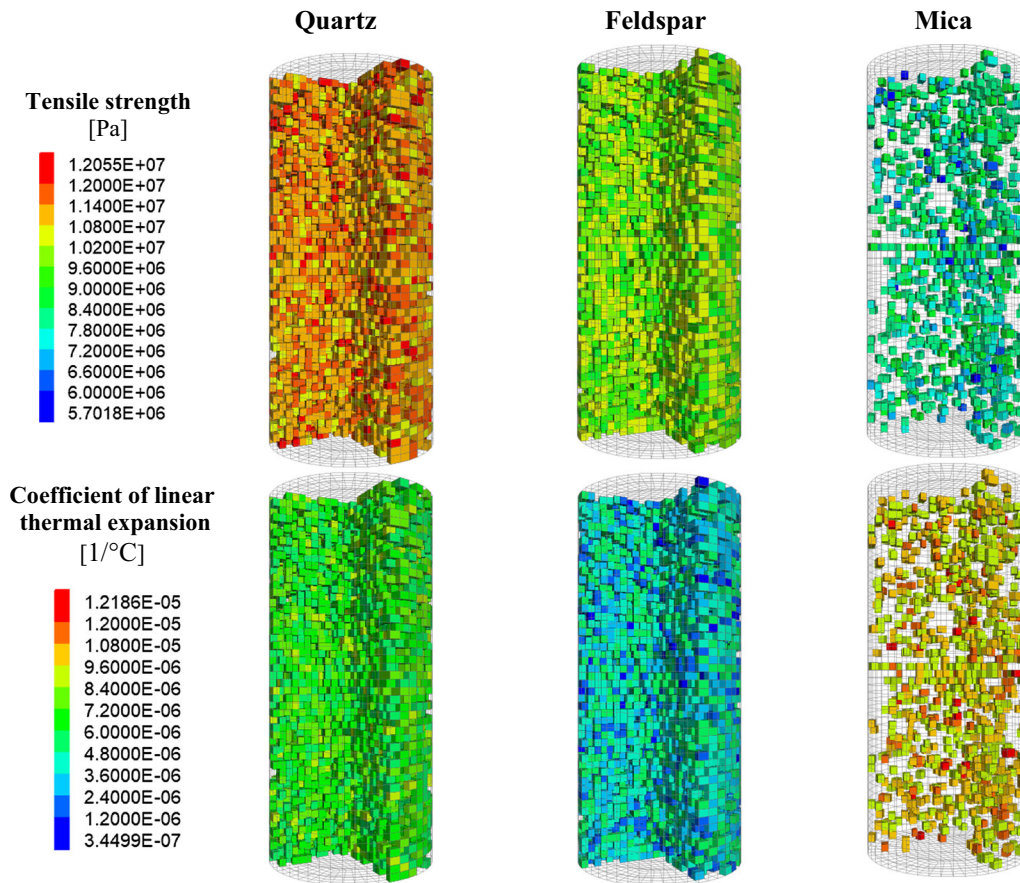


Fig. 11 Property distributions of different minerals at room temperature

interact with each other and are widespread across the whole sample. In a continuum numerical model, the macrocracks can be represented by a certain values of plastic strain (see Fig. 12b, d). It is visible that the crack patterns of the simulations are in good agreement with the laboratory test observations in terms of macrocracks, if a strain value of about 0.09 is interpreted as macroscopic crack.

Although the macrocracks are only visible above certain temperatures, change in p-wave velocity and open porosity (Fig. 3) indicate that microcracks induced by thermal stresses occur much earlier. Johnson et al. [15] has also found that thermal cracking occurs when a certain threshold temperature is exceeded, which is different for different rocks (e.g. 75 °C for Westerly granite and 200 °C for Sioux quartzite). They also found that thermal cracking increases progressively after threshold temperature, and the preponderance of cracking occurs below the quartz transition temperature of 573 °C. This trend is also observed in our simulations. Figure 13 shows the variation of p-wave velocity (laboratory testing) and the number of failed elements (i.e. element with plasticity states) at different temperatures in the simulation. Failed elements can be interpreted as thermally induced

microcracks. Their evolution in time shows a reverse tendency compared to the development of p-wave velocity. The quantity of induced cracks is increasing with increasing temperature, and more than about 80% of the cracks are induced before 600 °C. Figure 14 shows the plasticity states (i.e. microcracks) and plasticity tension strain (cracks with certain widths) on the axial plane of the cylindrical sample. The crack initiation temperature is about 80 °C with a few randomly induced microcracks across the sample. The element failures begin to occur progressively after the threshold temperature. Most elements fail in tension in the temperature range from 80 to 1000 °C. However, at about 500 °C shear failure begins to develop quickly with increasing temperature (see Fig. 14a).

The obvious macrodamage cannot be observed directly with naked eyes before a certain high temperature (e.g. 1000 °C) is reached (Fig. 14b), because the widening of the pre-induced cracks happens at higher temperatures. Laboratory tests have shown that below the quartz transition temperature of 573 °C, the decrease in p-wave velocity is associated with microcrack evolution, but above 573 °C, new crack formation is relatively seldom, and the p-wave velocity decrease is mainly caused by the widening

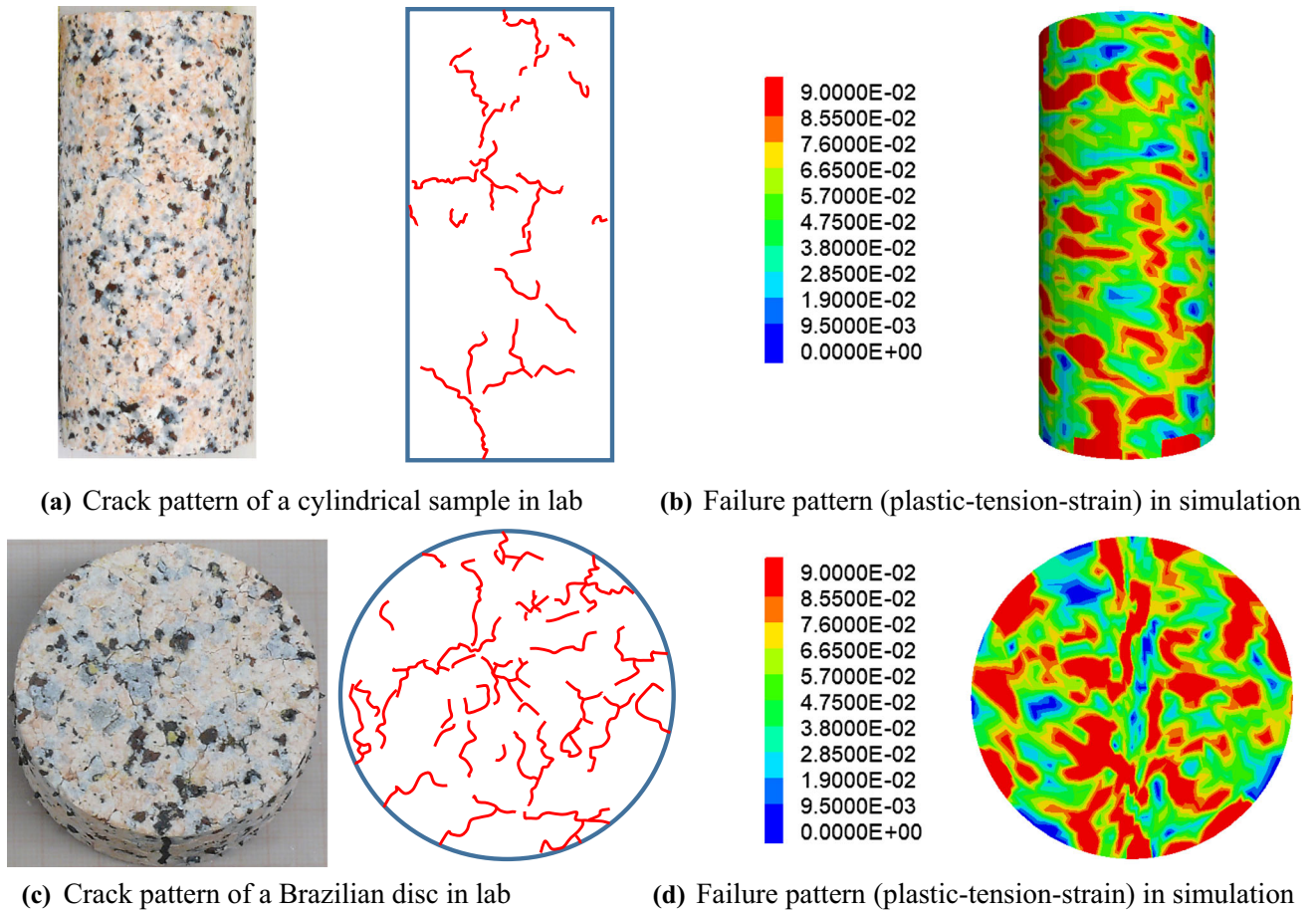


Fig. 12 Thermal-induced macrocracks of granite samples after 1000 °C heat treatment

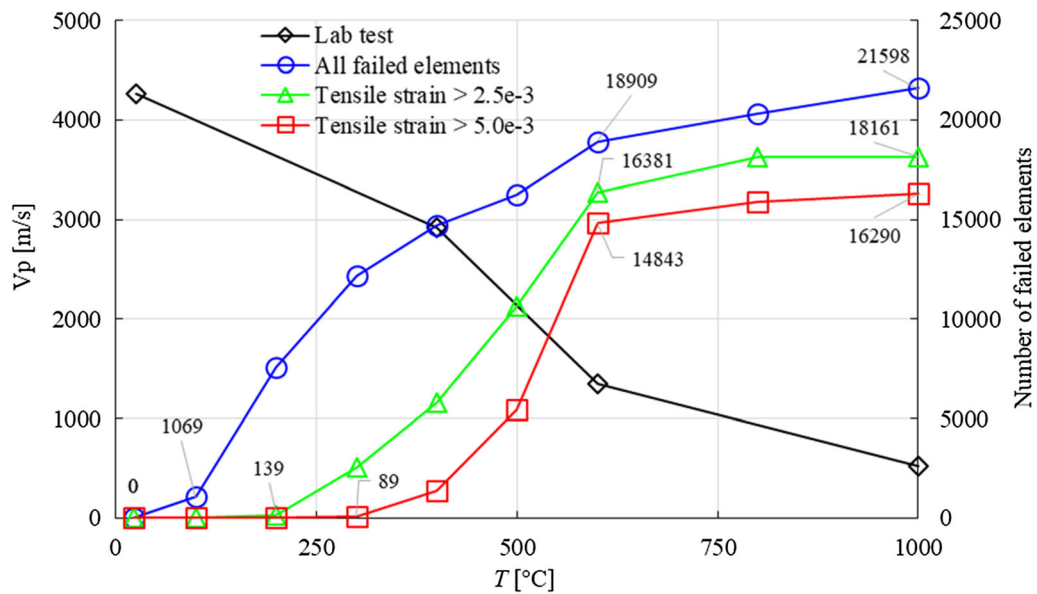


Fig. 13 Variation of p-wave velocity and number of failed elements at different temperatures

of earlier formed microcracks [1, 15, 16]. When plastic tensile strain in a failed element > 2.5e-3, the number of

cracks widened by thermal stresses is much smaller than for cracks with tensile strain > 0 (the blue line in Fig. 13).

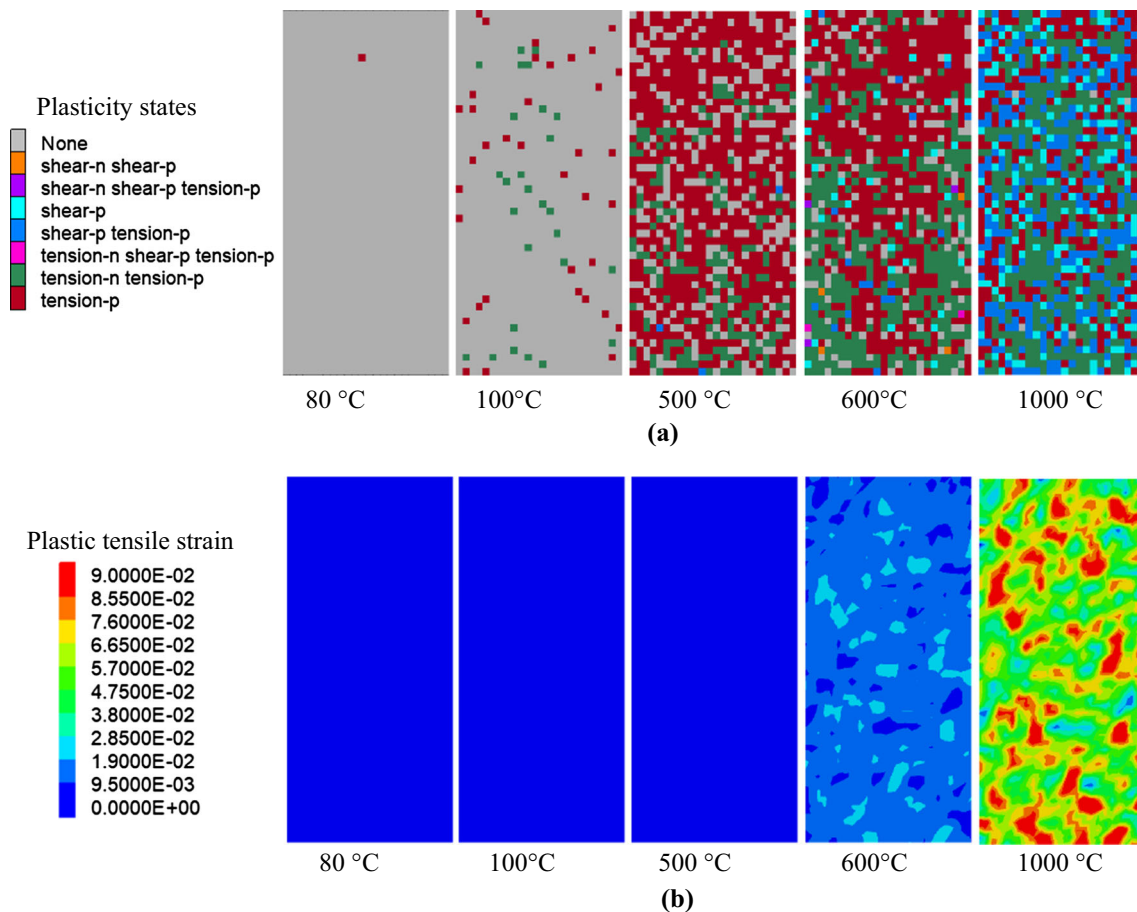


Fig. 14 Failed elements and plastic tensile strain at elevated temperatures

This trend becomes more obvious for cracks with tensile strain $> 5e-3$. In particular, around 573 °C, the number of widened cracks shows the sharpest increase. After 600 °C, both, the decreasing rate of p-wave velocity and the increasing rate of number of failed elements show a simultaneous reduction. Therefore, it is concluded that the majority of newly created thermal cracks occurs in the range between 100 °C and 600 °C. The dominant impact of the α - β quartz transition is widening of pre-existing cracks rather than the formation of new microcracks.

4.4.2 Granite strength after heat treatment

After cooling down to room temperature, the granite samples were mechanically loaded. Figure 15 compares the ultimate failure modes of granite samples before and after heating as observed in laboratory test and numerical simulations. The comparison of the failure modes of granite without and after heating (take 1000 °C as an example) indicates a significant influence of temperature treatment on failure behaviour. At room temperature, the granite shows typically brittle behaviour, and the samples split into several parts. For samples heated to 1000 °C, the

cylindrical samples are crushed into fine pieces producing extended shear zones rather than sharp, single failure planes. At room temperature, Brazilian disc is perfectly split in two parts through a tensile fracture in the loading plane, while the lateral parts of the specimen remain fairly undamaged. However, after heating to 1000 °C in addition to the main fracture which still will split the Brazilian disc into two parts, a multiple fracturing process with many minor, secondary cracks is observed (compare Figs. 12c, d, 15g, h). The failure modes obtained by the numerical simulation are quite similar to those documented by the laboratory tests. This confirms the accuracy and reliability of the proposed numerical modelling.

To better understand the mechanical behaviour, the axial stress–strain curves of cylindrical granite models are plotted in Fig. 16. Before heating, the granite samples show a typical brittle stress–strain behaviour. Strength and brittleness are gradually lost at elevated temperatures, especially after 600 °C. Samples heated up to 800 °C and 1000 °C show a clear ductile behaviour. These trends are consistent with the laboratory test results (see Fig. 4). Figure 17 compares uniaxial compression and tensile strength obtained by laboratory tests and simulations.

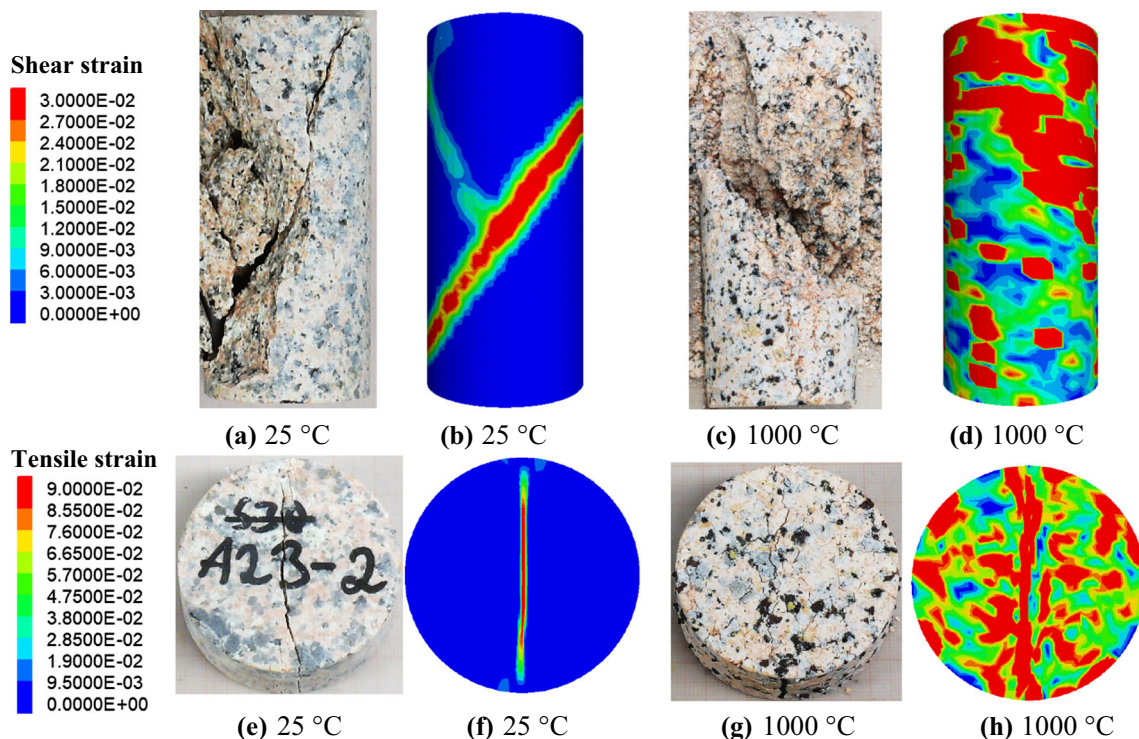


Fig. 15 Comparison of failure patterns of specimens after mechanical tests in laboratory and simulation

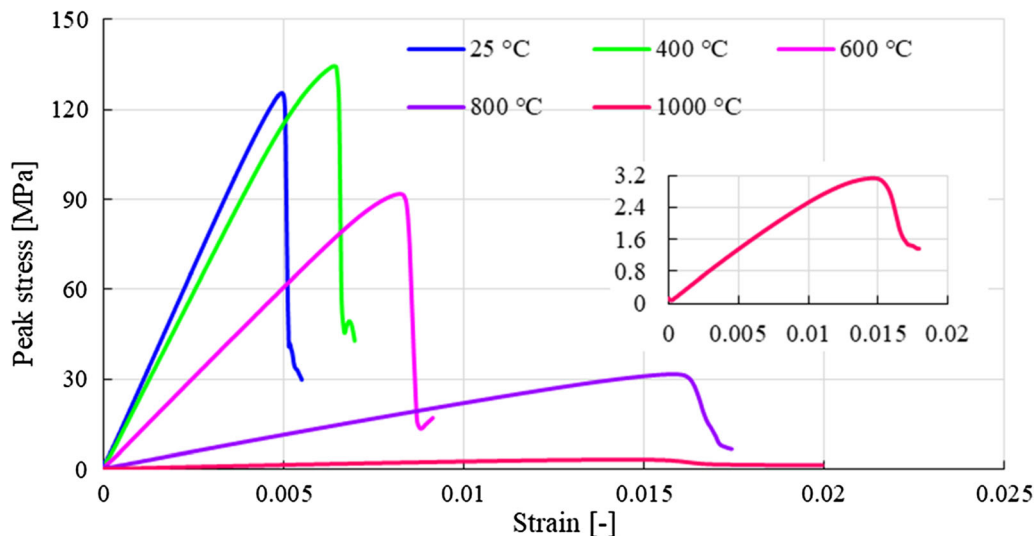


Fig. 16 Axial stress–strain curves of uniaxial compression tests (simulations)

Crack density and width show a strong increase after the threshold temperature of 80 °C (see Figs. 13, 14, 18), because the tensile strength of granite shows a decrease with increasing temperature (see Fig. 17b). However, UCS does not show a decrease up to about 400 °C although the number of failed elements keeps increasing. As Fig. 18 clearly shows, shear failure only is dominant in samples previously treated at temperatures beyond 400 °C. Therefore, we can deduce that

obvious UCS reduction in granite due to heating is mainly caused by increasing shear failure.

5 Conclusion

A series of laboratory tests was conducted on Eibenstock granite. Cylindrical specimens and discs prepared for Brazilian tensile tests were thermally treated by

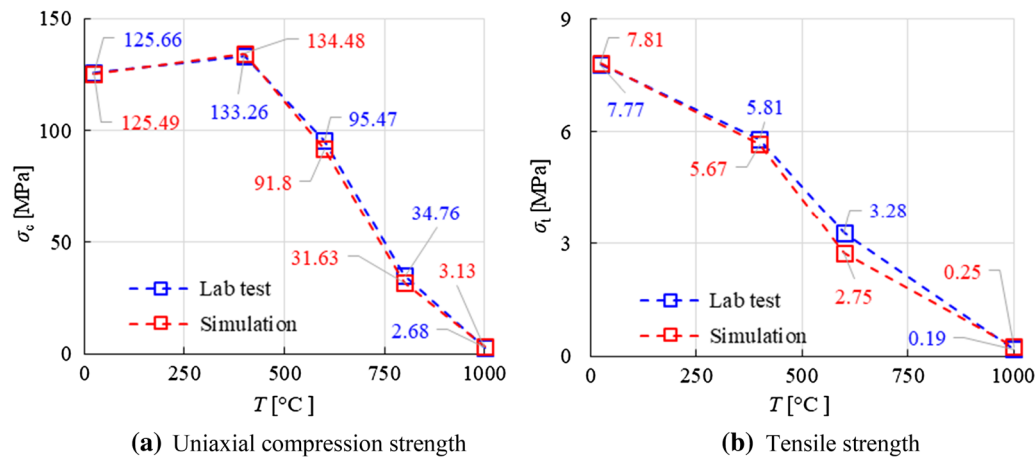


Fig. 17 UCS and tensile strength measured at room temperature after heating to certain temperatures

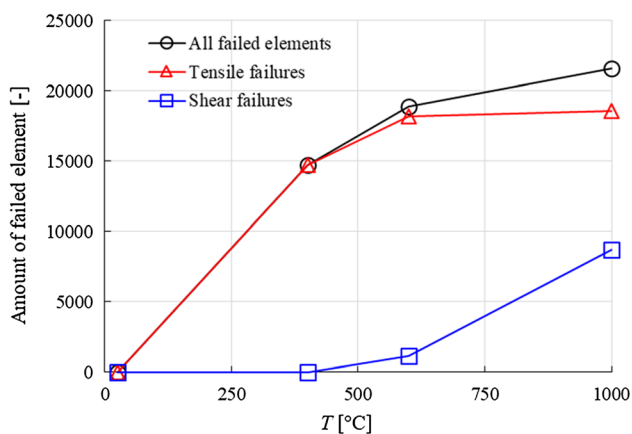


Fig. 18 Amount of different types of failed elements at elevated temperatures

temperatures up to 1000 °C using a heating rate of 5 °C/min. Physical and thermo-mechanical properties were measured before and after the heat treatment. Continuum-based numerical models were built representing cylindrical samples and Brazilian discs with heterogeneous properties to increase the understanding of thermo-mechanical behaviour influenced by high-temperature treatments. Based on laboratory tests and numerical simulation, the following conclusions can be drawn.

1. The density of Eibenstock granite shows a slight decrease with increasing temperature mainly caused by thermal volume increase. P-wave velocity decreases with rising temperature, with the most significant decrease caused by the α - β quartz transition. Open porosity shows an opposite trend compared to the p-wave velocity. The biggest increase in creation of open pores is observed in the temperature range from 600 to 1000 °C indicating that more cracks are

connected than new cracks induced in this temperature range.

2. Although the granite can still keep brittle failure characteristics at lower temperatures, the samples above 800 °C obviously show ductile failure behaviour. The UCS of granite increases slightly before decreasing rapidly up to 1000 °C. However, the peak axial strain at failure always shows an increase with increasing temperature. The threshold Young's modulus relating stress and strain at failure state shows that the stiffness of the granite decreases continuously with increasing temperature. This trend is similar to the tensile strength evolution at elevated temperatures.
3. The specific heat capacity increases linearly up to 600 °C and then drops slightly at higher temperatures. Thermal conductivity and thermal diffusivity show a similar trend and decrease monotonically with increasing temperature. Both, the average and true coefficient of linear thermal expansion show first a sharp increase at the α - β quartz transition and experience a second increase in the temperature range between 870 and 980 °C.
4. A constitutive model was implemented into the code FLAC^{3D} to simulate the thermal-induced damage of granite at high temperatures. Statistical methods combined with real mineral composition were used to characterize the heterogeneity of the rock. The corresponding thermo-mechanical properties were assigned to the elements (grains) accordingly. The simulation results show a good agreement with the laboratory test results. The simulations can reproduce thermal-induced micro- and macrocracks, as well as the stress-strain behaviour and the final failure pattern.
5. Both, laboratory tests and simulations show that thermal-induced macrocracks can be observed by the naked eye at about 1000 °C. Though these cracks are

isolated, they interact and are widespread across the whole sample. Simulation reveals that microcracks induced by thermal stress occur much earlier at a threshold temperature of about 80 °C. Thermal cracking increases progressively after the threshold temperature, and the preponderance of newly formed cracks is created below the α - β quartz transition temperature. These microcracks are randomly generated across the whole sample. Although most thermal-induced damages are tensile failures, shear failure begins to develop quickly beyond 500 °C and becomes significant thereafter. UCS reduction in granite during heating is mainly caused by increasing shear failure. The simulation results also indicate that the dominant impact of α - β quartz transition is widening of pre-existing cracks rather than the formation of new microcracks.

Acknowledgements The first author would like to thank China Scholarship Council (CSC) (Grand No. 201606420069) for financial support doing research in Germany. Thanks for Mr. Wang Tongsheng in Wuhan University of Science and Technology for his help in testing the thermal conductivity.

Funding Open Access funding enabled and organized by Projekt DEAL.

Open Access This article is licensed under a Creative Commons Attribution 4.0 International License, which permits use, sharing, adaptation, distribution and reproduction in any medium or format, as long as you give appropriate credit to the original author(s) and the source, provide a link to the Creative Commons licence, and indicate if changes were made. The images or other third party material in this article are included in the article's Creative Commons licence, unless indicated otherwise in a credit line to the material. If material is not included in the article's Creative Commons licence and your intended use is not permitted by statutory regulation or exceeds the permitted use, you will need to obtain permission directly from the copyright holder. To view a copy of this licence, visit <http://creativecommons.org/licenses/by/4.0/>.

References

- Bauer SJJ, Johnson B (1979) Effects of slow uniform heating on the physical properties of the westerly and charcoal granites. In: Proceedings of 20th US symposium rock mechanics, pp 7–18
- Chen W, Konietzky H (2014) Simulation of heterogeneity, creep, damage and lifetime for loaded brittle rocks. *Tectonophysics* 633:164–175. <https://doi.org/10.1016/j.tecto.2014.06.033>
- Chen Y, Wang S, Ni J et al (2017) An experimental study of the mechanical properties of granite after high temperature exposure based on mineral characteristics. *Eng Geol* 220:234–242. <https://doi.org/10.1016/j.enggeo.2017.02.010>
- DIN EN 1936 (2007) Natural stone test method—determination of real density and apparent density, and of total and open porosity. Deutsches Institut für Normung [DIN], Berlin, Germany
- Dwivedi RD, Goel RK, Prasad VVR, Sinha A (2008) Thermo-mechanical properties of Indian and other granites. *Int J Rock Mech Min Sci* 45:303–315. <https://doi.org/10.1016/j.ijmms.2007.05.008>
- Freire-Lista DM, Fort R, Varas-Muriel MJ (2016) Thermal stress-induced microcracking in building granite. *Eng Geol* 206:83–93. <https://doi.org/10.1016/j.enggeo.2016.03.005>
- Griffiths L, Lengliné O, Heap MJ et al (2018) Thermal cracking in westerly granite monitored using direct wave velocity, coda wave interferometry, and acoustic emissions. *J Geophys Res Solid Earth* 123:2246–2261. <https://doi.org/10.1002/2017JB015191>
- Hartlieb P, Toifl M, Kuchar F et al (2016) Thermo-physical properties of selected hard rocks and their relation to microwave-assisted comminution. *Miner Eng* 91:34–41. <https://doi.org/10.1016/j.mineng.2015.11.008>
- Heuze FE (1983) High-temperature mechanical, physical and thermal properties of granitic rocks: a review. *Int J Rock Mech Min Sci Geomech Abstr* 20:3–10
- Hidnert P, Dickson G (1945) Some physical properties of mica. *J Res Natl Bur Stand* 35:309–353
- ISRM (1978) Suggested methods for determining tensile strength of rock materials. *Int J Rock Mech Min Sci Geomech Abstr* 15:99–103
- ISRM (1979) Suggested methods for determining the uniaxial compressive strength and deformability of rock materials. *Int J Rock Mech Min Sci Geomech Abstr* 16:137–140. [https://doi.org/10.1016/0148-9062\(79\)91450-5](https://doi.org/10.1016/0148-9062(79)91450-5)
- Itasca (2019) FLAC3D fast Lagrangian analysis of continua in 3 dimensions—FLAC3D 7.0 documentation
- James JD, Spittle JA, Brown SGR, Evans RW (2001) A review of measurement techniques for the thermal expansion coefficient of metals and alloys at elevated temperatures. *Meas Sci Technol* 12:R1–R15. <https://doi.org/10.1088/0957-0233/12/3/201>
- Johnson B, Gangi AF, Handin J (1978) Thermal cracking of rock subjected to slow, uniform temperature changes. In: Proceedings of 19th US symposium rock mechanics, vol 19, pp 259–267. [https://doi.org/10.1016/0148-9062\(79\)91483-9](https://doi.org/10.1016/0148-9062(79)91483-9)
- Lin W (2002) Permanent strain of thermal expansion and thermally induced microcracking in Inada granite. *J Geophys Res Solid Earth* 107:6. <https://doi.org/10.1029/2001JB000648>
- Liu HY, Roquete M, Kou SQ, Lindqvist PA (2004) Characterization of rock heterogeneity and numerical verification. *Eng Geol* 72:89–119. <https://doi.org/10.1016/j.enggeo.2003.06.004>
- Nordlund E, Zhang P, Dineva S, Saiang C, Mainali G (2014) Impact of fire on the stability of hard rock tunnels in Sweden. *Stiftelsen bergteknisk forskning-Befo*, Stockholm, Sweden. ISSN: 1104-1773. http://www.befonline.org/UserFiles/Archive/443/BeFo_Rapport_136_skyddad.pdf
- Otto C, Kempka T (2015) Thermo-mechanical simulations confirm: temperature-dependent mudrock properties are nice to have in far-field environmental assessments of underground coal gasification. *Energy Procedia* 76:582–591. <https://doi.org/10.1016/j.egypro.2015.07.875>
- Polyakova IG (2014) The main silica phases and some of their properties. In: Schmelzer JWP (ed) *Glass: selected properties and crystallization*. De Gruyter, Berlin, pp 197–268
- Robertson EC (1988) *Thermal properties of rocks*. US Department of Interior Geology Survey, pp 88–441
- Saiang C, Miskovsky K (2011) Effect of heat on the mechanical properties of selected rock types—a laboratory study. In: 12th ISRM congress. International society for rock mechanics and rock engineering
- Shao S, Wasantha PLP, Ranjith PG, Chen BK (2014) Effect of cooling rate on the mechanical behavior of heated Strathbogie granite with different grain sizes. *Int J Rock Mech Min Sci* 70:381–387. <https://doi.org/10.1016/j.ijmms.2014.04.003>
- Siegesmund S, Snethlage R (2013) *Stone in architecture*, 4th edn. Springer, Berlin

25. Tan X, Konietzky H, Frühwirt T (2014) Laboratory observation and numerical simulation of permeability evolution during progressive failure of brittle rocks. *Int J Rock Mech Min Sci* 68:167–176. <https://doi.org/10.1016/j.ijrmms.2014.02.016>
26. Tan X, Konietzky H, Chen W (2016) Numerical simulation of heterogeneous rock using discrete element model based on digital image processing. *Rock Mech Rock Eng* 49:4957–4964. <https://doi.org/10.1007/s00603-016-1030-0>
27. Tham LG, Cheung YK, Tang CA (2001) Numerical simulation of the failure process of rocks. *Tamkang J Sci Eng* 4:239–252
28. Tribaudino M, Angel RJ, Cámara F et al (2010) Thermal expansion of plagioclase feldspars. *Contrib Min Petrol* 160:899–908. <https://doi.org/10.1007/s00410-010-0513-3>
29. Vales F, Rezakhanlou R (1999) Determination of the fracture mechanical parameters of porous ceramics from microstructure parameters measured by quantitative image analysis. *J Mater Sci* 4:4081–4088. <https://doi.org/10.1023/A:1004632503249>
30. Wang F, Konietzky H (2019) Thermo-mechanical properties of granite at elevated temperatures and numerical simulation of thermal cracking. *Rock Mech Rock Eng*. <https://doi.org/10.1007/s00603-019-01837-1>
31. Wang F, Frühwirt T, Konietzky H, Zhu Q (2019) Thermo-mechanical behaviour of granite during high-speed heating. *Eng Geol* 260:105258. <https://doi.org/10.1016/j.enggeo.2019.105258>
32. Wang F, Konietzky H, Herbst M (2019) Influence of heterogeneity on thermo-mechanical behaviour of rocks. *Comput Geotech* 116:103184. <https://doi.org/10.1016/j.compgeo.2019.103184>
33. Weinhold S (2018) Changes of mechanical properties and mineralogical composition of Eibenstock granite through thermal treatment (in German). Technische Universität Bergakademie Freiberg
34. Wen H, Lu JH, Xiao Y, Deng J (2015) Temperature dependence of thermal conductivity, diffusion and specific heat capacity for coal and rocks from coalfield. *Thermochim Acta* 619:41–47. <https://doi.org/10.1016/j.tca.2015.09.018>
35. Yan C, Jiao Y (2019) A 2D discrete heat transfer model considering the thermal resistance effect of fractures for simulating the thermal cracking of brittle materials. *Acta Geotech*. <https://doi.org/10.1007/s11440-019-00821-x>
36. Yan C, Zheng H (2017) A coupled thermo-mechanical model based on the combined finite-discrete element method for simulating thermal cracking of rock. *Int J Rock Mech Min Sci* 91:170–178. <https://doi.org/10.1016/j.ijrmms.2016.11.023>
37. Yang SQ, Tian WL, Huang YH (2018) Failure mechanical behavior of pre-holed granite specimens after elevated temperature treatment by particle flow code. *Geothermics* 72:124–137. <https://doi.org/10.1016/j.geothermics.2017.10.018>
38. Yu Q, Zhu W, Ranjith PG, Shao S (2018) Numerical simulation and interpretation of the grain size effect on rock strength. *Geomech Geophys Geoenergy Georesour* 4:157–173. <https://doi.org/10.1007/s40948-018-0080-z>
39. Zhao Z (2016) Thermal influence on mechanical properties of granite: a microcracking perspective. *Rock Mech Rock Eng* 49:747–762. <https://doi.org/10.1007/s00603-015-0767-1>
40. Zhu C, Arson C (2014) A thermo-mechanical damage model for rock stiffness during anisotropic crack opening and closure. *Acta Geotechnol* 9:847–867. <https://doi.org/10.1007/s11440-013-0281-0>
41. Zhu Z, Tian H, Mei G et al (2019) Experimental investigation on physical and mechanical properties of thermal cycling granite by water cooling. *Acta Geotechnol*. <https://doi.org/10.1007/s11440-019-00898-4>

Publisher's Note Springer Nature remains neutral with regard to jurisdictional claims in published maps and institutional affiliations.